Monthly Notices of the ROYAL ASTRONOMICAL SOCIETY

MNRAS **532,** 1966–1979 (2024) https://doi.org/10.1093/mnras/stae1539
Advance Access publication 2024 June 20

Overcoming confusion noise with hyperspectral imaging from PRIMAger

J. M. S. Donnellan,[1]★ S. J. Oliver,[1] M. Béthermin,[2,3] L. Bing,[1] A. Bolatto,[4] C. M. Bradford,[5,6] D. Burgarella,[3] L. Ciesla,[3] J. Glenn,[7] A. Pope,[8] S. Serjeant [9], R. Shirley,[10] J. D. T. Smith [11] and C. Sorrell[9]

[1]*Astronomy Centre, University of Sussex, Falmer, Brighton BN1 9QH, UK*
[2]*Université de Strasbourg, CNRS, Observatoire astronomique de Strasbourg, UMR 7550, F-67000 Strasbourg, France*
[3]*Aix Marseille Univ, CNRS, CNES, LAM, 13388 Marseille, France*
[4]*Department of Astronomy, University of Maryland, College Park, MD 20742, USA*
[5]*NASA Jet Propulsion Laboratory, 4800 Oak Grove Dr, Pasadena, CA 91011, USA*
[6]*California Institute of Technology, 1200 E California Blvd, Pasadena, CA 91125, USA*
[7]*NASA Goddard Space Flight Center, Greenbelt, MD 20771, USA*
[8]*Department of Astronomy, University of Massachusetts, Amherst, MA 01003, USA*
[9]*School of Physical Sciences, The Open University, Walton Hall, Milton Keynes, MK7 6AA, UK*
[10]*Max Planck Institut für Extraterrestrische Physik, Giessenbachstrasse 1, D-85748 Garching, Germany*
[11]*Ritter Astrophysical Research Center, University of Toledo, Toledo, OH 43606, USA*

Accepted 2024 June 18. Received 2024 June 18; in original form 2024 April 10

ABSTRACT

The PRobe far-Infrared Mission for Astrophysics (PRIMA) concept aims to perform mapping with spectral coverage and sensitivities inaccessible to previous FIR space telescopes. PRIMA's imaging instrument, PRIMAger, provides unique hyperspectral imaging simultaneously covering 25–235 μm. We synthesize images representing a deep, 1500 h deg^{-2} PRIMAger survey, with realistic instrumental and confusion noise. We demonstrate that we can construct catalogues of galaxies with a high purity (>95 per cent) at a source density of 42 k deg^{-2} using PRIMAger data alone. Using the `XID+` deblending tool, we show that we measure fluxes with an accuracy better than 20 per cent to flux levels of 0.16, 0.80, 9.7, and 15 mJy at 47.4, 79.7, 172, and 235 μm, respectively. These are a factor of ∼2 and ∼3 fainter than the classical confusion limits for 72–96 and 126–235 μm, respectively. At $1.5 \leq z \leq 2$, we detect and accurately measure fluxes in 8–10 of the 10 channels covering 47–235 μm for sources with $2 \lesssim \log(\mathrm{SFR}) \lesssim 2.5$, a 0.5 dex improvement on what might be expected from the classical confusion limit. Recognizing that PRIMager will operate in a context where high-quality data will be available at other wavelengths, we investigate the benefits of introducing additional prior information. We show that by introducing even weak prior flux information when employing a higher source density catalogue (more than one source per beam), we can obtain accurate fluxes an order of magnitude below the classical confusion limit for 96–235 μm.

Key words: galaxies: photometry – infrared: galaxies.

1 INTRODUCTION

The process of star formation is integral to understanding galaxy evolution (e.g. Madau & Dickinson 2014). However, a significant fraction of the UV emission from hot massive stars, which trace star formation, is obscured by dust and re-emitted at far-infrared (FIR) wavelengths (Cardelli, Clayton & Mathis 1989; Calzetti et al. 2000; Burgarella et al. 2013a).

Previous studies have attempted to derive FIR-related properties of galaxies and correct for dust attenuation in order to determine physical properties without directly observing in the FIR, e.g. using the IRX-β relation to determine IR luminosity (Meurer, Heckman & Calzetti 1999) or using energy-balancing SED fitting procedures to determine star formation rates (SFR) and dust attenuation (Małek et al. 2018). However, there is no clear agreement within the literature that such approaches are universally applicable or accurate, e.g. with deviations from the IRX-β relation being found (Narayanan et al. 2018) as well as discrepancies between SFRs and dust attenuation values obtained when fitting SEDs with and without IR photometry (Riccio et al. 2021; Pacifici et al. 2023).

Moreover, the total emission we receive from galaxies in the infrared, the cosmic infrared background (CIB; Puget et al. 1996), forms roughly half of the total extragalactic background light (e.g. Hauser & Dwek 2001; Dole et al. 2006). The discovery of this high CIB, along with wide-field FIR and sub-mm surveys, revealed a population of galaxies that are heavily enshrouded in dust and are known as dusty star-forming galaxies (see Casey, Narayanan & Cooray 2014, for a review). The most luminous DSFGs are thought to be the most intense stellar nurseries in the Universe, with incredibly high SFRs (Rowan-Robinson et al. 2018), and are therefore of crucial importance when it comes to understanding the cosmic star-

★ E-mail: j.donnellan@sussex.ac.uk

formation history of the Universe (Long et al. 2023). Observations at short wavelengths can detect DSFGs, but they may be misidentified as unobscured galaxies at higher redshifts (e.g. Zavala et al. 2023). Statistical studies of populations of these DSFGs show clearly that their FIR luminosity is significant at most epochs and dominates the luminosity density of the universe at some (e.g. Gruppioni et al. 2013a; Burgarella et al. 2013b).

Observations across the FIR wavelength range are therefore required in order to better characterize and constrain the physical properties of galaxies. However, due to the opacity of the atmosphere for much of the FIR wavelength range, these observations must be conducted either from the stratosphere or space. Previous space-based FIR observatories have each significantly enhanced our understanding of the dusty Universe but have also been limited in their capabilities. The first spaced-based telescope to survey the full sky at IR wavelengths was the *Infrared Astronomical Satellite* (*IRAS*; Neugebauer et al. (1984)), but was only able to conduct shallow observations, detecting only the most luminous IR galaxies (LIRGS). *The Infrared Space Observatory* (*ISO*; Kessler et al. 1996) provided spectroscopy at IR wavelengths (see Genzel & Cesarsky 2000, for a review) but was limited to observing the local Universe due to low sensitivity. Imaging and spectroscopy from the Spitzer Space Telescope (Werner et al. 2004) greatly advanced our understanding of obscured star-formation, with the *Spitzer/MIPS* 24 μm emission widely used as a tracer of obscured luminosity and SFR (Reddy et al. 2008; Elbaz et al. 2011; Shivaei et al. 2017). *Spitzer*, however, was ultimately limited to only five years of cold mission, and its spectroscopy was mainly limited to wavelengths below 35 μm. The *Herschel Space Observatory* (Pilbratt et al. 2010) significantly extended the survey parameter space, discovering extreme DSFGs (e.g. Riechers et al. 2013) and was able to further constrain the CIB (Viero et al. 2015; Béthermin et al. 2017; Duivenvoorden et al. 2020) and the evolution of the IR luminosity function (Gruppioni et al. 2010, 2013b) but could only image in a small number of broad-bands. Overall, however, these past missions were limited in imaging to a small number of broad-bands, which were not able to capture all the features across the IR range. Previous IR spectroscopy suffered from limited sensitivity or wavelength coverage.

Imaging data from these previous observatories were also limited in depth due to what is known as confusion noise (particularly *Spitzer/MIPS* (Dole et al. 2004) and *Herschel/SPIRE* (Nguyen et al. 2010)). FIR space-based telescopes suffer from poor angular resolution due to the limited mirror sizes, which leads to the blending of sources when the telescope beam is large compared to their average separation. This gives rise to confusion noise, which increases with the observed wavelength for a given mirror size.

Identifying the need to improve upon our coverage of the FIR sky, NASA released an Announcement of Opportunity (AO) for an Astrophysics Probe Explorer limited to two themes as recommended by the National Academies' 2020 Decadal Review, one of which being a far-infrared imaging or spectroscopy mission. In response to this call, the PRobe far-infrared Mission for Astrophysics (PRIMA) concept mission has been developed.[1] PRIMA is a 1.8 m space-based telescope that will be cryogenically cooled to 4.5 K. This FIR observatory has two planned instruments; the Far-Infrared Enhanced Survey Spectrometer (FIRESS) and the PRIMA Imaging Instrument (PRIMAger). FIRESS is a spectrometer covering the 24–235 μm wavelength range in four grating modules with spectral resolution $R = \lambda/\Delta\lambda \sim 100$. A high resolution mode will allow it to reach R of thousands across full band. The PRIMAger instrument is composed of two bands. The first offers hyperspectral imaging with a $R \sim 10$ providing 12 independent flux measurements from 25 to 80 μm while the second provides four broad-band filters between 96 and 235 μm, all sensitive to polarization. Both instruments will operate with 100 mK cooled kinetic inductance detectors allowing for an incomparable improvement of sensitivity in FIR. As an observatory PRIMA will cover a wide range of science topics such as, but not limited to, origins of planetary atmospheres, evolution of galaxies and build-up of dust and metals through cosmic time (Moullet et al. 2023).

PRIMAger will be able to provide significantly improved sensitivity compared to previous FIR spaced-based imaging instruments, e.g. by over ∼2 orders of magnitude for point sources compared to *Herschel/PACS* (see Section 2.2 for more details on PRIMAger sensitivity capabilities). However, to realize the full benefit from this sensitivity, it will be essential to reduce the impact of confusion.

Various statistical methods have been developed to overcome the problems presented by confusion when estimating fluxes from FIR maps. One such tool is `XID+`, developed by Hurley et al. (2017). It is a deblending tool that uses a probabilistic Bayesian framework in which to include prior information on galaxy positions and fluxes and to obtain the full posterior probability distribution for fluxes. Positional priors can come from short-wavelength FIR maps, or from catalogues at other (e.g. near-R) wavelengths. Hurley et al. (2017) found that `XID+` performs better on flux accuracy and flux uncertainty accuracy for simulated SPIRE maps than previous prior-based source extraction tools, such as `DESPHOT` and `LAMBDAR` (e.g. `XID+` at 10 mJy had similar accuracy to `LAMBDAR` at 70 mJy), and has been utilized in performing source extraction for the Herschel Extragalactic Legacy Project (HELP; Shirley et al. 2019, 2021) and is now a tool used in the wider community (e.g. Shim et al. 2023).

This paper will demonstrate that by utilizing the flux modelling capabilities of `XID+`, accurate flux measurements of galaxies can be obtained below the classical confusion limit from simulated PRIMAger maps. In Section 2, we outline how the simulated PRIMAger maps are generated and the confusion noise is estimated. Blind source detection is performed on the maps in Section 3 to produce prior catalogues with positions to be used to de-blend the confused maps. In Section 4, we explore how prior information affects the flux modelling of `XID+`. In Section 5, we show how `XID+` performs in terms of measured flux accuracy across the whole simulated data set and compare to the classical confusion limits. We then discuss the implications of these results on which galaxies we are able to determine the physical properties of in Section 6 and make final conclusions in Section 7.

2 SIMULATIONS

2.1 Simulated PRIMAger maps

To test how well PRIMAger will recover fluxes of sources in the presence of confusion noise, we utilize simulated PRIMAger maps generated by Béthermin et al. (2024) (hereafter referred to as B24) using the Simulated Infrared Dusty Extragalactic Sky (SIDES) simulation (Béthermin et al. 2017). The SIDES simulation, map generation process, estimation of baseline confusion limits, and simple blind detection of sources in the absence of instrumental noise are all described and presented in B24; however, we summarize some of the relevant information here.

PRIMAger will be able to conduct hyperspectral imaging with linear variable filters in two bands, PHI1 and PHI2, between 25 and

[1] https://prima.ipac.caltech.edu/

Table 1. Properties and detection limits in the 12 representative PRIMAger channels for the two hyperspectral bands, PHI1 and PHI2, and the four polarimetry broad-band channels, PPI1–PPI4. Beam FWHMs are estimated (column 3) for the baseline telescope aperture (1.8 m) and detector and pixel layout. The point source sensitivities are given (column 4) for a deep survey observed for ∼1500 h deg^{-2} in the absence of confusion. The classical confusion limit as estimated by B24 is also quoted (column 5) for each channel. This is defined as 5 times the confusion noise, which is obtained by estimating the variance in each of the maps via an iterative clipping process in the absence of instrumental noise. The depth of each Wiener-filtered catalogue of monochromatic, blind detections at the 95 per cent purity level is presented (column 6) with details discussed in Section 3.2. The depth reached by the two runs of XID+ with two different prior catalogues are also provided (columns 7 and 8) and are discussed in Section 5. The *Wiener-filtered* prior catalogue is self-consistently derived from Wiener-filtered catalogues extracted from the synthetic data, the *Deep* prior catalogue comes from the input model and represents a prior catalogue from other observatories with weak flux priors. XID+ depths are the limiting fluxes defined in equation (3). N.B. the flux accuracy tolerance in the purity analysis of the Wiener-filtered catalogue is different from than used in the definition of XID+ limiting flux. Thus, their values are not directly comparable. Data are quoted to three significant figures.

Channel	Central wavelength [μm]	Estimated beam FWHM [″]	Sensitivity ($5\sigma_{\rm inst}$) [μJy]	Classical confusion ($5\sigma_{\rm conf}$) [μJy]	Wiener-filtered catalogue depth (95 per cent purity) [μJy]	XID+ depth, Wiener-filtered prior ($5\sigma_{\rm MAD}$) [μJy]	XID+ depth, Deep prior, ($5\sigma_{\rm MAD}$) [μJy]
PHI1_1	25.0	4.1	70	20	55	93	82
PHI1_2	27.8	4.3	79	27	61	107	86
PHI1_3	30.9	4.6	88	37	69	121	93
PHI1_4	34.3	4.9	99	51	79	138	108
PHI1_5	38.1	5.2	114	71	94	162	116
PHI1_6	42.6	5.7	134	107	117	181	149
PHI2_1	47.4	6.2	83	161	87	163	95
PHI2_2	52.3	6.7	94	249	115	209	117
PHI2_3	58.1	7.3	108	401	160	271	138
PHI2_4	64.5	8.0	123	667	225	387	167
PHI2_5	71.7	8.8	153	1120	336	602	229
PHI2_6	79.7	9.7	172	1850	521	801	285
PPI1	96.3	11.6	29	4520	770	1680	281
PPI2	126	15.0	45	12300	2002	4090	747
PPI3	172	20.3	67	28 400	5037	9700	2650
PPI4	235	27.6	82	46 000	18 023	14 600	7030

80 μm with $R \sim 10$. For simplicity, we represent each of these bands with six continuous channels spanning the wavelength range of the band (PHI1_1 to PHI1_6 for band PHI1 and PHI2_1 to PHI2_6 for band PHI2). PRIMAger will also be able to image with polarimetry via four broad-band channels (PPI1–PPI4), centred at 96, 126, 172, and 235 μm with $R \sim 4$ sensitive to three angles of polarization (see B24 for further discussion of PRIMAger's polarimetry capabilities). Table 1 includes the central wavelengths and estimated beam full width at half-maxima (FWHM) for each of the 12 representative channels for bands PHI1 and PHI2 as well as the four polarimetry channels. PRIMAger will be able to observe simultaneously with all bands; however, due to their relative position on the focal plane, all bands observe different parts of the sky and mapping is needed to cover a region of interest.

SIDES is a simulation of the extragalactic sky in the far-infrared and the millimetre domain, starting from a dark-matter halo light-cone with galaxy properties generated using a semi-empirical model. It is able to reproduce a large set of observed galaxy properties, such as the source number counts at various angular resolutions, the redshift distributions, and the large-scale anisotropies of the CIB. For this work, the latest version of the simulation presented in Béthermin et al. (2022) is used and includes the spatial clustering of galaxies. The effect of clustering on the confusion noise estimates is investigated by B24.

The output from the SIDES simulation is a light-cone catalogue of $1.4^\circ \times 1.4^\circ$, $0 < z < 10$, corresponding to a comoving volume of 0.17 Gpc^3 containing 5.6 M galaxies. The catalogue also contains the fluxes of each source, which are obtained by integrating the spectral energy distribution of the SIDES galaxies over the representative PRIMAger channels. Simulated maps that contain confusion noise but no instrumental noise are generated for each of the 16 channels (hereafter, these maps are referred to as 'noiseless maps', with simulated instrumental noise being added to produce 'noisy maps' as described in Section 2.2). The noiseless maps are generated by attributing the flux of the sources to the centre of the pixels at which they are located and then convolving the map with the relevant beam profile. The beam profiles are assumed to be Gaussian with FWHM values given in Table 1. Map pixel sizes are 0.8, 1.3, and 2.3 arcsec for bands PHI1, PHI2, and PPI, respectively. Cut-outs of the same region from the simulated PRIMAger maps in six of the channels are shown in Fig. 1, with the effect of confusion noise clearly demonstrated as you move to longer wavelengths, whereby sources become increasingly blended. The estimation of the confusion noise from the maps containing no instrumental noise is discussed below.

2.1.1 *Estimating classical confusion noise*

Confusion noise arises due to surface brightness fluctuations in the maps arising from the astronomical sources themselves, convolved with the telescope beam. The lowest flux at which an individual point-like source can be identified above that fluctuating background is called the confusion limit (Condon 1974). In order to estimate the confusion limit of a simulated noiseless PRIMAger map, B24 applied a 5σ-clipping process. The standard deviation, σ, of all pixels is computed, 5σ positive outliers are masked, and the standard deviation of the unmasked pixels is recomputed. This process is iterated until the standard deviation converges, giving the $1\sigma_{\rm conf}$ confusion noise. The *classical* confusion limit is then defined as 5 times this confusion noise, values of which are given in Table 1 for each of the PRIMAger channels.

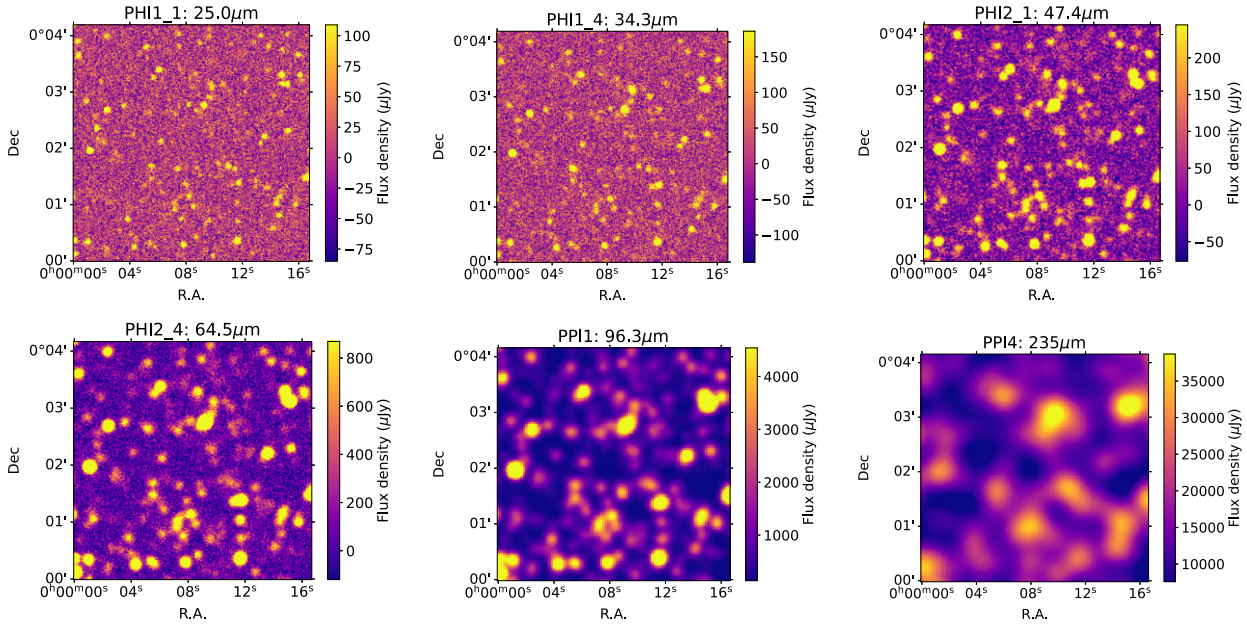

Figure 1. Simulated PRIMAger maps including both 'instrumental noise' and source confusion, illustrating the transition from instrumental dominated at short wavelengths to confusion dominated at longer wavelengths. The sources are drawn from the SIDES simulations. The instrumental noise synthesizes observations of 1500 h deg^{-2} and is discussed in Section 2.2. Cutouts are 4 × 4 arcmin in representative channels with $R = 10$ in bands PHI1 and PHI2 and $R = 4$ in band PPI.

2.2 PRIMAger sensitivities and simulated noise

With significantly improved sensitivity compared to previous FIR space-based telescopes, PRIMAger will reach a point source sensitivity of 220 and 300 μJy in bands PHI1 and PHI2, respectively, at the 5σ level with integration time 10 h deg^{-2}. Likewise, it will reach point source sensitivities of 200, 300, 400, and 500 μJy in bands PPI1, PPI2, PPI3, and PPI4, respectively. For comparison, the *deepest* surveys with *Herschel* at 110, 160, and 250 μm (close to the PPI2, PPI3, and PPI4 bands) reached 5σ sensitivities of 1100, 2100, and 3800 μJy in (see table 5 in Oliver et al. 2012)

In order to make realistic PRIMAger maps, we add instrumental[2] noise to the simulated maps. We assume a deep, 1500 h deg^{-2} survey which is expected to give 5σ point source sensitivities of 88, 108, 29, 45, 67, and 82 μJy in bands PHI1, PHI2, PPI1, PPI2, PPI3, and PPI4, respectively.

We add Gaussian noise to each pixel based on the nominal point source sensitivities (5$\sigma_{\rm inst}$) for the considered survey design for each PRIMAger channel in Table 1. We assume no spatially correlated noise and that the instrumental noise is constant across each respective map. Maps which contain both confusion noise and this added instrumental noise are referred to as 'noisy maps' for the remainder of the paper.

3 SOURCE DETECTION

XID+ deblends maps using the positions of known sources (Section 4.1) and therefore requires a catalogue containing their prior positions. Usually, such a prior catalogue is obtained from shorter wavelength ancillary data from other telescopes, as was done by Pearson et al. (2018) who used optical data in the COSMOS field to deblend *Herschel/SPIRE* maps with XID+. However, to demonstrate that it is possible to detect sources and accurately measure their fluxes entirely from PRIMAger data in a self-contained way, a source detection process is run on the simulated PRIMAger maps themselves. This is possible due to the wide spectral coverage of PRIMAger, particularly in the PHI1 band (25–43 μm). This band is not limited by confusion and allows for sources to be detected at multiple wavelengths. Additionally, this band will capture PAH emission lines from star-forming sources around cosmic noon, enhancing their detection probability.

In order to explore the impact of different prior knowledge on the flux accuracy of XID+ (Section 4.2), we consider two different source detection methods.

3.1 Blind detection without instrumental noise

A blind source detection algorithm performed on all of the noiseless PRIMAger maps by B24, who produced a catalogue of 101 540 sources from the 1.96 deg^2 maps. The basic algorithm they employ searches for local maxima within a 5 × 5 pixel region. The threshold was set to be 5 times the measured confusion noise.

3.2 Blind detection on wiener filtered maps with instrumental noise

In far-IR and submillimetre blind surveys, it is common to perform blind detection by cross-correlating the signal with the PSF of the instrument. This method is expected to maximize the signal-to-noise ratio (S/N) on isolated point sources with white noise. This is appropriate for shallow surveys, dominated by instrumental noise. However, for the deep observations planned for PRIMA on extragalactic deep fields, the spatially correlated confusion noise is non-negligible even in the shortest PHI1 bands and starts to dominate the noise in the data at PHI2 and longer wavelengths. PSF matching filter, in this case, no longer maximizes the S/N of point sources; rather, it increases the confusion noise and reduces the completeness of blind detection.

[2]The non-confusion noise in PRIMAger maps arises from multiple sources, including the detectors and photon statistics; for convenience, we aggregate these and refer to them as 'instrumental noise'.

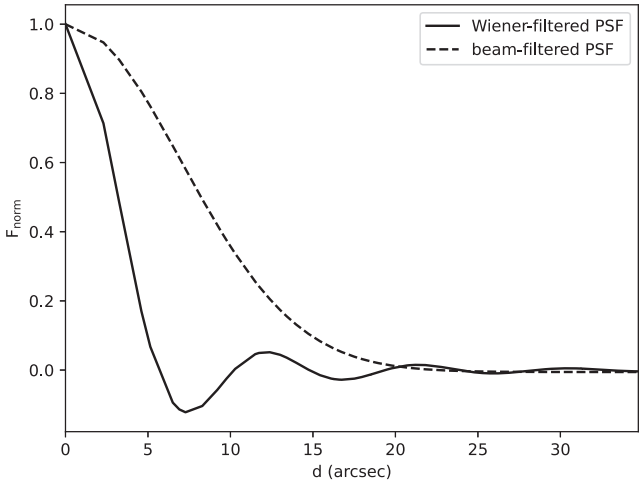

Figure 2. The effective Point Spread Function (PSF) profile in a PPI1 image after applying a Wiener filter (solid line) or a näive PSF filter (dashed line). The näive filter is optimal for flux estimation of isolated point sources, including non-local data with reduced weight, to enhance the signal-to-instrumental noise ratio in comparison to a central, purely local estimate. The Wiener filter has a much narrower central beam, which provides some reduction in instrumental noise but is balanced against adding confusion noise from non-local data. The Wiener filter also has a negative feature (at around 7 arcsec in this example), which provides a local background subtraction, actively reducing confusion noise.

To maximize the S/N of blind source detection in data with substantial confusion noise, previous blind far-IR and millimetre surveys have introduced a Wiener filter as the general form of matching filter kernel that optimize point source blind detection on confusion-limited data (Chapin et al. 2011; Geach et al. 2017; Shirley et al. 2021). The philosophy of this method is a compromise between the uncorrelated white instrumental noise (which benefits from a wider kernel) and other spatially correlated confusion noise (which benefits from a narrower kernel and local background removal) to maximize the S/N ratio of point source blind detection. Our construction of Wiener filter follows the principles in Chapin et al. (2011) and the similar frameworks of constructing blind catalogue in HELP project (Shirley et al. 2021). We refer the readers to those references for details but summarise the outcomes of the match-filtering as follows.

We consider the total noise in the simulated data from PRIMAger observations as two main components: a white noise component coming from the instrumental noise and a confusion noise component coming from other point sources in the map. In each band, we take the instrumental and confusion noise level expected for 1500-h PRIMAger deep survey over 1 deg^2, create the Wiener filters following Chapin et al. (2011), and derive the corresponding match-filtered map. A comparison between the effective PSF profile after applying Wiener filter and instrument PSF filter to the simulated PRIMA observation is illustrated in Fig. 2. The effective PSFs after Wiener filtering have primary peaks narrower than the instrument PSF, this reduces source blending and improve sthe completeness of blind source detection in confusion-dominated PHI2 and PPI1-PPI4 bands. The higher order ringings feature from Wiener filtering introduces additional fake sources around in blind detection, which we identify and remove later. However, the impact of ringing is limited to regions around very bright sources, and the corresponding fake sources could be removed based our knowledge on their relative intensity compared to the nearest bright sources.

The blind source detection in the match-filtered maps is made using the find_peak method provided by `photutils`. A source is identified if the central pixel is the maximum among all pixels in a 5 × 5 pixel region. The maps are calibrated following Chapin et al. (2011) in mJy/Beam, such that the point source flux could be estimated directly from the peak.

To remove false sources created by Wiener filtering, we examined all sources in the simulation that are bright enough to produce ringing features above the total noise level of the map, $\sigma_{\rm total}$, ($\sigma^2_{\rm total} = \sigma^2_{\rm inst} + \sigma^2_{\rm conf}$, where $\sigma_{\rm inst}$ and $\sigma_{\rm conf}$ are the instrumental noise and the confusion noise, respectively). We then predict the expected intensity of the corresponding ringing features. Sources with fluxes less than five times the expected ringing feature intensity are considered as contaminated and removed from the blind detection catalogue. We note that although this conservative cut could also remove some real faint sources, this will be reflected in our completeness and flux accuracy estimates, and further optimization could improve our results.

Before constructing the prior list, it is critical to define a cut on the depth for blindly detected source catalogs to avoid significant contamination from false detections, while maintaining high completeness. Significant contamination could be a problem not because of the false objects themselves but also, through the `XID+` modelling, reduce the flux accuracy for real sources.

Far-IR and submillimeter surveys usually set a flux cut based on the purity derived from statistical analysis. Purity is defined as the fraction of detected source above certain flux limit that have corresponding counterparts in the simulated input catalogue close enough in positions and fluxes. In our analysis, we consider that a correct counterpart to a blindly detected source satisfies the following criteria (similar to B24):

(i) the positional offset between blindly detected source and the counterpart, $d_{\rm off}$, satisfies $d_{\rm off} \leq \theta_{\rm FWHM}/2$, where $\theta_{\rm FWHM}$ is the FWHM of the instrument PSF

(ii) the observed flux ($S_{\rm obs}$) of the blindly detected source and the true flux ($S_{\rm True}$) of the counterpart satisfies $S_{\rm True}/2 \leq S_{\rm obs} \leq 2S_{\rm True}$

(iii) the counterpart is the brightest source that satisfies criteria (i) and (ii).

We cross-match the blind detected source catalogue with the simulation input catalogues using those criteria. For each band, we perform cross-matching on blindly detected sources with S/N> 2.5. The purity of blindly detected sources above different flux limits are then derived accordingly. We choose a cut in observed flux corresponding to the 95 per cent purity and the flux threshold for each band are listed in Table. 1. The resulting blindly detected single-band catalogue reaches completeness of ∼83 per cent at PHI1 bands, ∼67 per cent at PHI2 bands, and ∼75 per cent at PPI1–PPI4 bands on sources with $S_{\rm True} > \sigma_{\rm total}$. These catalogues are further cross-matched from the shortest to the longest wavelength to obtain a unique list of priors from Wiener filtering.

4 XID+ AND PRIOR INFORMATION

4.1 XID+: A probabilistic De-Blender

`XID+`[3], developed by Hurley et al. (2017), is a prior-based source photometry tool which is able to simultaniously estimate the fluxes of a collection of sources with known positions. The basic model of

[3]https://github.com/H-E-L-P/XID_plus

XID+ assumes that the input data (d) are maps with $n_1 \times n_2 = M$ pixels, where the maps are formed from N known sources, with flux densities $\boldsymbol{S_i}$ and a background term accounting for unknown sources. The point response function (PRF, P) quantifies the contribution each source makes to each pixel in the map and is assumed to be a Gaussian. The map can therefore be described as follows:

$$\boldsymbol{d} = \sum_{i=1}^{N} \boldsymbol{P}\,\boldsymbol{S_i} + N(0, \Sigma_{\rm inst}) + N(B, \Sigma_{\rm conf}), \quad (1)$$

where the two independent noise terms represent the instrumental noise and the residual confusion noise, which is modelled as Gaussian fluctuations about B, a global background. XID+ undertakes an MCMC sampling from this probabilistic model to obtain the full posterior. Originally, Hurley et al. (2017) utilised the Bayesian inference tool, Stan, to perform the MCMC sampling. However, here we implement the Numpyro backend, which is built into XID+ because it is faster.

The original XID+ applied a flat, uniform prior on the source fluxes (from zero flux to the highest pixel value in the map). However, later works (Pearson et al. 2017, 2018; Wang et al. 2021) demonstrated that by applying more informative flux priors, e.g. from SED-fitting of ancillary photometry, provided improvements in flux accuracy and allowed fainter fluxes to be reliably measured.

We would expect the choice of prior information provided to affect the modelling accuracy. In the basic XID+ model described above, the possible prior informations to include are (a) the positions of previously detected sources (i.e. the density of sources) and (b) the prior probability distributions of their fluxes. The following section investigates the impact of varying these two prior information dimensions on the flux modelling accuracy of XID+.

4.2 Impact of prior knowledge

In order to investigate the impact of the inclusion of prior knowledge on the modelling accuracy of XID+, we consider (a) varying the density of sources included in the prior source position catalogue as well as (b) varying the prior flux distribution. One would expect the flux modelling accuracy to improve as the density of the prior source position catalogue increases. As more faint sources are included in the modelling, fewer sources remain to contribute confusion. However, without any prior flux knowledge, there would be an upper limit, and even a reversal, to the gain in modelling accuracy as the number of prior sources increases due to degeneracies being introduced to the model. With prior flux knowledge, these degeneracies may be overcome.

We consider three prior source position catalogues of varying source densities:

(i) **B24 catalogue**: discussed in Section 3.1
(ii) **Wiener-filtered catalogue**: discussed in Section 3.2
(iii) **Deep catalogue**: Here, we apply a simple flux cut to the full SIDES simulation catalogue, keeping sources which have a flux greater than 1 μJy in the PHI1_1 band. This produces a catalogue of 588 550 sources, corresponding to a source density of ∼3.5 sources/beam in the PPI1 channel.

A summary of these catalogues is presented in Table 2. Note that when considering application to real data, (i) could, in principle, be generated from PRIMager map data if sufficiently deep that instrumental noise was negligible; (ii) could be generated from the PRIMager survey data we are considering here; (iii) would require catalogues generated from data from other telescopes.

Table 2. Number of sources in each of the three prior source catalogues over 1.96 deg^2 explored in Section 4.2. B24 uses a basic peak detection on noise-free (confusion only) maps; the Wener-filtered catalogue is an extraction from a simulation of the deep, 1500 h deg^{-2}, survey; the Deep catalogue comes from the simulated input catalogue and represents a prior catalogue from other facilities. The source density is given as number of sources per band PPI1 beam. The corresponding flux depth from the simulation input catalogue at this source density is also provided.

Name	No. of galaxies	Source density [sources/beam] (in band PPI1)	Flux depth [μJy]
B24	101 540	0.60	270
Wiener-filtered	82 575	0.49	369
Deep	588 550	3.50	12.9

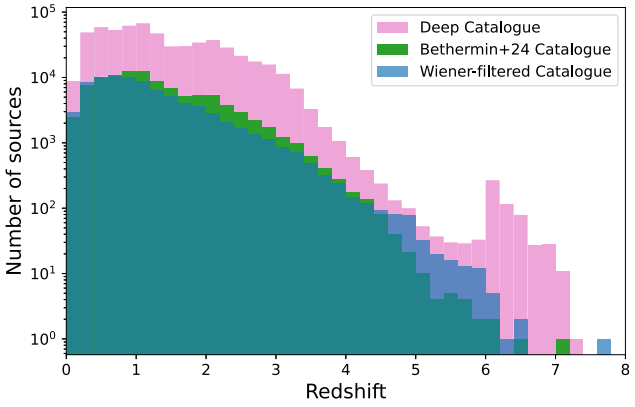

Figure 3. Redshift distribution for the three prior source catalogues considered in Section 4.2: The Deep catalogue (pink) of ∼590 000 sources which all have a flux greater than 1 μJy in the PHI1_1 channel, the catalogue of blindly detected sources in the noiseless maps (green) from B24 of ∼102 000 sources and the catalogue of blindly detected sources in the Wiener-filtered, noisy maps (blue) with ∼83 000 sources.

The redshift distributions of the sources in each of the above catalogues are shown in Fig. 3. A secondary peak of sources in the deep catalogue is present at $z \gtrsim 6$ due to the 3.3 μm PAH emission line moving into the PHI1_1 channel, which is used for the selection of sources for this particular catalogue. Fig. 4 shows where the sources from each catalogue lie in the SFR-stellar mass plane for a single redshift bin ($1.5 < z \leq 2.0$) compared to values for the star-forming main-sequence (MS) from the literature (Speagle et al. 2014; Pearson et al. 2018; Leslie et al. 2020; Leja et al. 2022). The Deep catalogue contains significantly more low-mass galaxies as well as a larger population of galaxies just below the MS, moving towards the quiescent region, across all masses. Conversely, the Wiener-filtered and B24 catalogues have a higher percentage of their total sources above the MS.

For each of the catalogues, XID+ is run on a sample of the data covering ∼0.12 deg^2 with uninformative, flat flux priors (i.e. with uniform flux priors on all sources ranging from zero to the highest pixel value in the respective map.) for the PPI1 channel. This channel is chosen as it is confusion-dominated (i.e. the instrumental noise is negligible compared to the confusion noise) but remains key for many of the PRIMA science goals. Additionally, XID+ was run with Gaussian flux priors centred on the sources' true flux, with standard deviations of 2.0, 1.0, 0.5, and 0.3 times the true flux of the sources (i.e. with increasing prior flux knowledge). In a real survey, these flux prior constraints would likely come from predicted fluxes

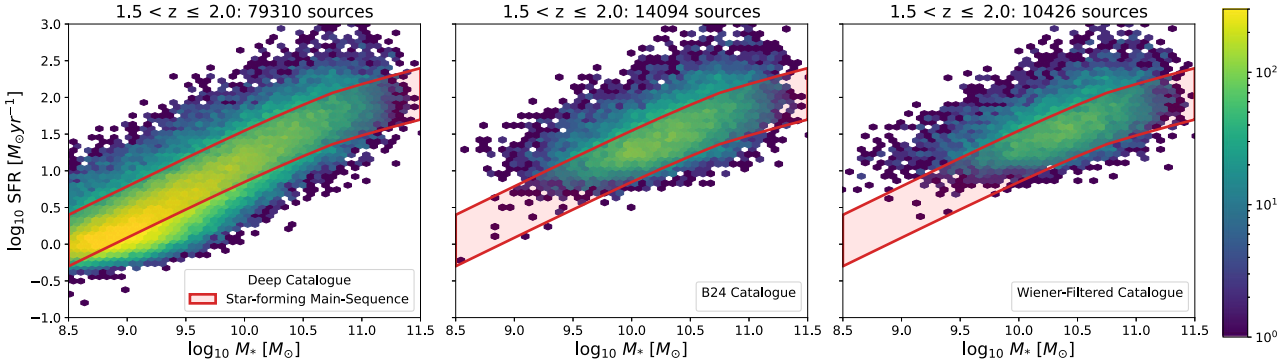

Figure 4. Location of sources within the three catalogues considered in Section 4.2 on the stellar mass-SFR plane for a single redshift bin of $1.5 < z \leq 2.0$. For reference, we indicate a range of reported locations for the star-forming 'main sequence' in the literature (Speagle et al. 2014; Pearson et al. 2018; Leslie et al. 2020; Leja et al. 2022). The number of sources in each M_*–SFR bin is shown by the colour scale for the Deep, B24 and Wiener-filtered catalogues in the left-hand, middle, and right-hand panels, respectively.

obtained from SED-fitting procedures utilizing ancillary photometry (Section 6.3 discusses this further). The method used for measuring the performance of the flux modelling from XID+ for the above runs as well as the subsequent results are described in the following section.

4.2.1 *Limiting flux statistic*

In order to quantify the flux accuracy of XID+ for the varying prior knowledge parameters, we define the following statistics to describe the 'limiting flux' reached in each of the PRIMAger maps. First, we quantify the deviation of the extracted fluxes, $S_{\rm obs}$ from the true fluxes, $S_{\rm true}$, within bins of true flux using the median absolute deviation (scaled to a Gaussian), $\sigma_{\rm MAD}$:

$$\sigma_{\rm MAD}(S_{\rm true}) = 1.4862 \cdot \text{Median}\left(\frac{\Delta S}{S_{\rm true}} - \text{Median}\left(\frac{\Delta S}{S_{\rm true}}\right)\right), \quad (2)$$

where $\Delta S = S_{\rm obs} - S_{\rm true}$. We then define the limiting flux, $S_{\rm limiting}$, as the flux at which $\sigma_{\rm MAD}$ equals 0.2:

$$S_{\rm limiting} = S_{\rm true}\Big|_{\sigma_{\rm MAD}=0.2}. \quad (3)$$

This corresponds to the true flux, at which the median deviation of the observed fluxes from the true values equals 20 per cent of the true flux. The choice of this statistic and whether it is a reasonable measure of the flux down to which source fluxes can be accurately recovered is considered in Appendix A.

The prior flux knowledge is quantified as the true flux, $S_{\rm true}$, over the dispersion in the Gaussian flux prior, $\sigma_{\rm prior}$. It is worth noting that the $S_{\rm true}/\sigma_{\rm prior} \sim 3.3$ flux prior is only considered in order to investigate the upper bound of this parameter space, as if we were able to constrain the flux a priori this accurately then new data would add little!

Fig. 5 shows the limiting flux in the PPI1 channel as a function of the prior flux knowledge for all three prior catalogues. It highlights how increasing the prior flux knowledge for the shallower prior source catalogues (the B24 and the Wiener-filtered catalogues) provides negligible gains. Therefore, it is better to only apply a flat flux prior to prior source catalogues of source densities <1. Increasing the prior flux knowledge at these source densities returns little gain but will likely introduce more assumptions into the modelling, depending on how the prior flux information is obtained. With no prior flux knowledge; however, the flux modelling accuracy can worsen if the

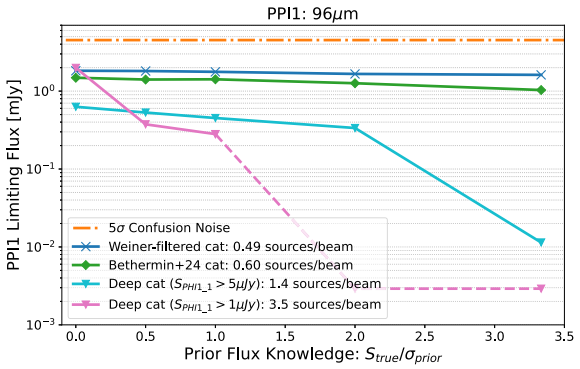

Figure 5. The limiting flux, as defined in Section 4.2.1, reached by XID+ in the PPI1 channel as a function of the prior flux knowledge. Prior knowledge is defined as the true flux of the sources, $S_{\rm true}$ divided by the spread on the Gaussian flux prior, $\sigma_{\rm prior}$ (i.e. as the prior flux knowledge increases, the spread on the flux prior decreases). Results are shown for a sample of the data (totalling $\sim$0.12 deg^2) from the three prior source catalogues described in Section 4.2: Weiner-filtered catalogue (green line with cross markers); blind detected catalogue from B24 (blue line with diamond markers); and the Deep catalogue (pink line with triangle markers). For the Deep catalogue beyond $S_{\rm true}/\sigma_{\rm prior} > 1$ (indicated by the dashed line), the limiting flux is $\sim$1 μJy, i.e. flux of the faintest source, indicating that the modelling is performing as well as possible. The effect of increasing the flux cut used to generate the Deep catalogue is illustrated by the cyan line with triangle markers. Source densities for each of the catalogues are indicated in the legend. The orange dash–dotted line shows the classical confusion limit for the PPI1 channel estimated by B24.

prior source density is too high due to the model becoming too complex and degenerate, as shown in Fig. 5. For these deeper, higher source density prior catalogues, even weak information from flux priors can break these degeneracies and lead to substantial gains in the XID+ flux modelling accuracy and limiting flux.

The Deep prior source catalogue considered here comprises all sources from the simulated catalogue brighter than 1 μJy in the PHI1_1 band. If one were to increase this flux cut, the prior catalogue would have a lower source density and would therefore result in an increase in the limiting flux for any given prior flux knowledge. This is illustrated by the cyan line with triangle markers in Fig. 5, which shows the increased limiting flux for the Deep catalogue with a higher flux cut of 5 μJy in the PHI1_1 band.

We note that Fig. 5 hints towards a critical point at which the XID+ flux modelling dramatically improves for a given prior source catalogue. If the prior catalogue is of a higher source density, then less prior flux knowledge is required to reach this critical point and vice versa. Investigating this parameter space of prior source density and prior flux knowledge with higher resolution than is considered within Fig. 5 is beyond the scope of this paper; however, it would likely provide further insights into the modelling capabilities of XID+.

4.3 Choice of prior source catalogue

To investigate the flux modelling performance of XID+ across the full simulated PRIMAger data set, we will continue with both the Wiener-filtered and the Deep prior source catalogues. The former will be used as the benchmark as it is generated from the more realistic maps, which include instrumental noise, providing a robust and conservative estimate of a realistic blind source detection process. No prior flux information will be used with this catalogue as to avoid introducing assumptions for little gain. This run will provide the most conservative limiting flux results.

The Deep prior source catalogue is not generated from PRIMAger's capabilities or from the maps themselves. However, a catalogue of such source density and depth is possible to obtain from wide-field surveys conducted by higher resolution observatories, such as The Nancy Grace Roman Space Telescope. It is important to understand how much can be gained from utilizing such rich ancillary data sets. Additionally for this run, we include prior flux information for each source as a Gaussian distribution centred on the true flux, $S_{\rm true}$, with a spread of $\sigma_{\rm prior} = S_{\rm true}$. This is to test the flux modelling performance in the more informative prior knowledge regime.

The blind detection catalogue produced by B24 represents what is possible to achieve in the limit of no instrumental noise (i.e. for very deep surveys). However, due to it being produced from the noiseless simulated PRIMAger maps, rather than the more realistic maps with added simulated noise that XID+ will be run on, it will not be considered further.

5 RESULTS

5.1 XID+ photometry with Wiener-filtered prior catalogue

Proceeding with the Wiener-channelled prior catalogue, we ran XID+ was run on each of the 16 noisy PRIMAger maps independently with flat flux priors. Note that the maps used as data input to XID+ are not filtered in any way; they are simply the simulated maps containing both confusion and instrumental noise (as described in Section 2.2). The output from XID+ is the full posterior distribution for the flux in the channel corresponding to the map of each source in the prior catalogue, including the correlation between sources. The measured flux of a given source for a particular channel is quoted as the median of its marginalised posterior flux distribution.

Fig. 6 shows the scaled MAD, $\sigma_{\rm MAD}$ (defined by equation (2)), of the measured fluxes from XID+ compared to true fluxes for all true source flux bins for the 10 reddest PRIMAger channels. It also shows the chosen 'limiting flux' threshold at $\sigma_{\rm MAD} = 0.2$, corresponding to a measured flux accuracy of 20 per cent (5σ), as defined in equation (3).

The limiting fluxes reached by XID+ in each of the 16 noisy PRIMAger maps are shown in Fig. 7 by the blue-dashed line. These are compared to the classical confusion limits for each map as calculated by B24 (solid orange line, also given in Table 1). For all six PHI1 maps, which are limited by the instrumental noise rather than the confusion noise, XID+ is able to accurately measure source

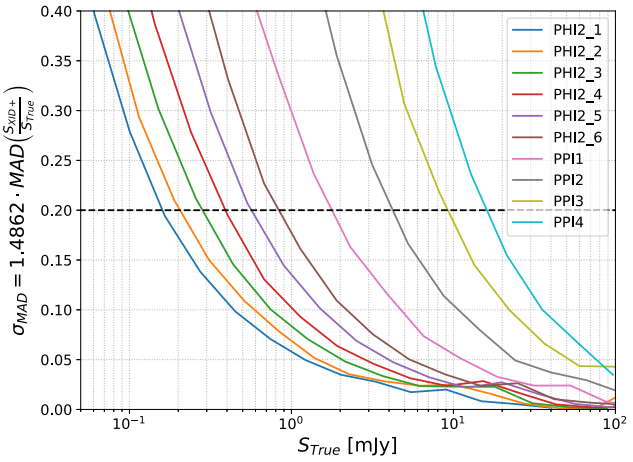

Figure 6. XID+ flux accuracy as a function of true flux for Wiener-filtered prior in the 10 reddest PRIMAger channels (coloured solid lines). Flux accuracy is quantified as the scaled median absolute deviation (MAD), $\sigma_{\rm MAD}$ as defined in equation (2), of the ratios of measured source fluxes from XID+. The horizontal black-dashed line shows the 'limiting flux' threshold at $\sigma_{\rm MAD} = 0.2$, which represents measured flux accuracy of 20 per cent (5σ). The true flux at which the coloured solid lines intercept with this threshold is taken to be the 'limiting flux' for the given channel, as defined in equation (3).

fluxes down to within a factor of 1.35 of the 5σ instrumental noise. For the remaining, redder maps, which are confusion-dominated (bands PHI2 and PPI), XID+ reaches a limiting flux below the classical confusion limit in each channel. As the bottom panel of Fig. 7 shows, the gain in depth relative to the classical confusion limit steadily increases through the representative channels of band PHI2. Starting at the PHI2_1 channel, accurate fluxes are recovered down to the confusion limit of this channel. By PHI2_6, fluxes that are a factor of $\sim$2 below the respective confusion limit are accurately recovered. For the 4 PPI channels (96–235 μm), this is improved to a factor of $\sim$3.

These results are also compared to two galaxy SED models from Kirkpatrick et al. (2015). One is a star-forming galaxy template at $z = 2$ and a luminosity of $L = 10^{12.3} L_{\odot}$ with no AGN emission contributing to the total IR luminosity (f_{AGN}= 0), shown by the dotted grey line in Fig. 7. The other SED template, however, has f_{AGN}= 0.4[4] and is shown by the solid grey line. Distinguishing between these two types of objects is important to the extragalactic science case for PRIMA. Being able to do so enables the study of the impact that AGN have on galaxy evolution. The limiting flux results from XID+ show that accurate fluxes can be obtained for both objects up to $\leq$100μm, spanning a range where there is significant distinction between these two SEDs.

5.2 XID+ photometry with deep prior catalogue

Fig. 7 also shows the results from the XID+ run with the Deep prior source catalogue with flux prior knowledge of $\sigma_{\rm prior}/S_{\rm true} = 1$ (pink-dash–dotted line). Utilizing these more informative priors allows for significantly deeper limiting fluxes to be reached, particularly for the PPI1–PPI3 channels, where the limiting flux is more than an order of magnitude below the classical confusion limits. Additionally, for

[4] $f_{\rm AGN}$ is the ratio of the AGN luminosity to the sum of the AGN and dust luminosities, $f_{\rm AGN} = L_{\rm AGN}/(L_{\rm dust} + L_{\rm AGN})$. In this case, the AGN SED is a type-2 AGN.

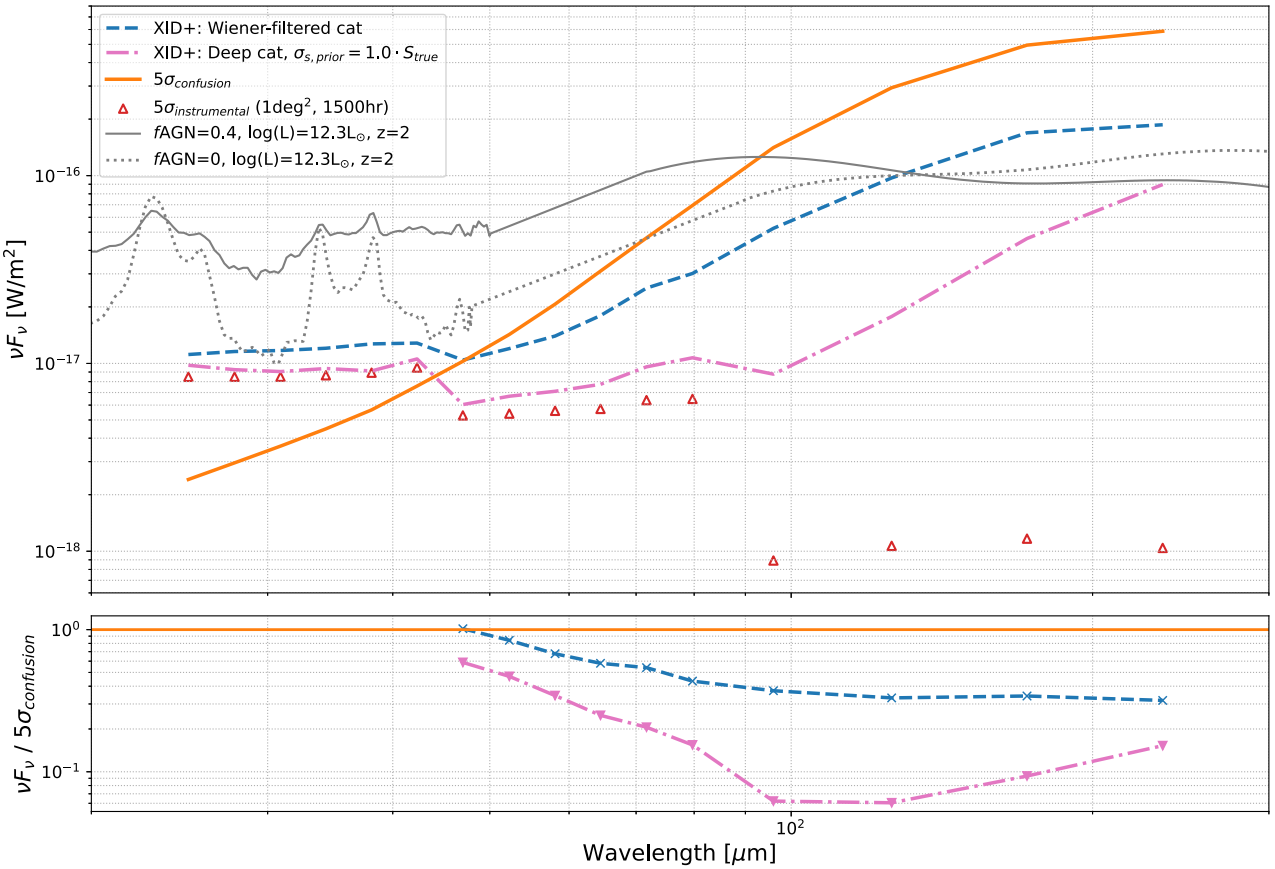

Figure 7. Limiting flux density as a function of wavelength from 25–235 μm for XID+ deblending. De-blending with positional and weak flux priors consistently attains 5σ depths more than an order of magnitude fainter than the classical confusion limit at $\lambda > 100$ μm. This figure shows that using XID+, SEDs from typical galaxies at $z = 2$ can be measured to $\lambda = 126$ μm using only positional priors (derived from the Wiener-filtered map) and out to the longest PRIMAger PPI channel (μ) with the addition of a weak intensity prior. **Top:** Limiting flux density as a function of wavelength covering the 12 representative channels of the two LVF PRIMAger bands, PHI1 (25–43 μm) and PHI2 (47–80 μm), and the 4 PPI channels (96–235 μm). Blue-dashed line shows the limiting flux density, as defined in Section 4.2.1, reached by XID+ with flat flux priors and the Wiener-filtered detection prior catalogue. The dash–dotted pink line shows the results from XID+ with the Deep prior catalogue and flux priors with $\sigma_{s,prior} = S_{true}$. The orange solid line shows the classical confusion limits from B24, and the red triangles show the 5σ baseline point source sensitives in each of the channels. Also plotted are two model SEDs of galaxies from Kirkpatrick et al. (2015) at $z = 2$ with luminosity $L = 10^{12.3} L_\odot$, corresponding to the knee of the FIR luminosity function at this redshift (Magnelli et al. 2013), and fraction of luminosity from AGN emission, f_{AGN}, of 0 and 0.4, shown by the dotted grey line and the solid grey line, respectively. **Bottom:** Limiting flux density reached by XID+ relative to the 5σ confusion limits for the 10 reddest channels which are confusion-dominated.

the PHI1 band and blue PHI2 channels, the limiting flux is pushed down to the instrumental noise of the simulated survey.

Comparing again against the two model SED templates with differing f_{AGN}, these deeper limiting fluxes allow for these two objects to be accurately observed in the two reddest PRIMAger channels (PPI3 and PPI4).

6 DISCUSSION

6.1 Alternative methods

In this paper, we have focused on quantifying how much fainter than the näive, classical confusion we can probe with PRIMAger using modern, but relatively well-established techniques. However, it is important to note that the hyperspectral capabilities of PRIMAger will lend themselves well to more sophisticated techniques, which are likely to do better. The rich spectral information available in PRIMAger (including the continuous linear variable filters in PH1 and PH2) can augment the spatial information. In this paper, we have concentrated on using the high resolution at short wavelengths to provide positional priors at longer wavelengths. However, this does not exploit the fact that different types of galaxies and galaxies at different redshifts have different spectral signatures. Simultaneously modelling the spatial and spectral information, which is possible in the XID+ framework, would improve these results. Even a relatively simple stepwise approach of stepping through the channels one-by-one and using the short wavelengths to inform the flux priors of the longer wavelengths would yield benefits (e.g. Wang et al. 2024, sub., and see Section 6.3). Furthermore, sophisticated tools are being developed rapidly in the context of AI and machine learning, and we note in Appendix B that impressive deconvolution results are not limited to this prior-based deblending technique but are a general property of the hyperspectral imaging data set.

PRIMager will also be working alongside spectral imaging capabilities from the FIRESS instrument. Tools like CIGALE (Boquien et al. 2019) can model simultaneously PRIMAger photometry and FIRESS spectral data allowing us to consistently model dust and gas.

It is also worth noting that our investigation has been restricted to deep surveys; future work is needed to assess wide surveys. As shown in B24, the wide-field surveys will also be affected by

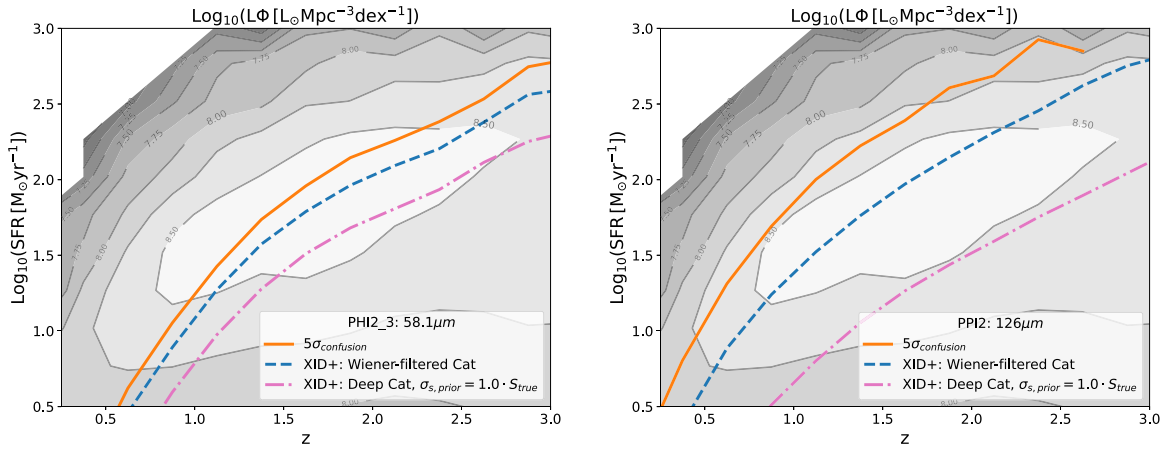

Figure 8. Regions of the redshift–SFR plane accessible to PRIMAger at the given limiting fluxes reached by XID+ in the PHI2_3 (left) and PPI2 (right) channels. Sources that lie within above the lines are those whose fluxes can be accurately measured in the given channels using XID+. Additionally, the FIR luminosity density as a function of redshift and SFR is shown by the grey-scale contours. The classical confusion limits from B24 in each channel are shown by the solid orange lines. The limiting fluxes from XID+ with the Wiener-filtered prior catalogue and the Deep prior catalogue with flux priors of $\sigma_{\rm s,prior} = S_{\rm true}$ are shown by the blue-dashed lines and the dash–dotted pink lines, respectively.

confusion, albeit to a lesser extent, and being confusion limited at longer wavelengths than the deep surveys. For the wide surveys, the reduced sensitivity at shorter wavelengths will have an impact on the prior catalogues that can be self-consistently constructed from PRIMA data, and hence the deblending performance. This can also be addressed by using multiband techniques in the detection process, e.g. generalizing the Wiener filtering to multibands.

6.2 Properties of galaxies accessible to PRIMAger

Having quantified how accurately we can measure fluxes and hence the flux limits at which we can accurately determine fluxes (i.e. to 'detect' galaxies), it is important to consider the implications for studies of galaxy properties. It is thus instructive to consider the detectability of galaxies in physical parameter space.

6.2.1 Redshift, SFR plane

We first consider the detectability of the significant star formation (as traced by the FIR luminosity density) as a function of SFR and redshift. The underlying FIR luminosity density of the SIDES simulation, $L\phi$, as a function of SFR and redshift is indicated by the grey-scale contours in Fig. 8. For each channel, we translate from a limiting flux from XID+ to a limiting SFR as follows. We select all sources from the SIDES simulation whose true fluxes are within 10 per cent of the limiting flux. The limiting SFR is defined as the median SFR of these sources.

These are shown in Fig. 8 for the limiting fluxes from the two XID+ runs with the Wiener-filtered and Deep prior catalogues by the blue-dashed and pink-dash–dotted lines, respectively, for two of the channels. The region of the z-SFR plane above these lines is where sources have fluxes in the given channel, which can be accurately measured for the given method.

The limiting boundary due to the confusion limit is also estimated in the same way (solid orange lines). As can be seen in the right-hand panel of Fig. 8, the confusion limit in the PPI2 channel prohibits sources that form the peak of the luminosity density from being reliably recovered. Utilizing XID+ allows for this peak to begin to be probed even with the low source density prior catalogue and no flux prior information. With the more extensive prior catalogue with additional prior flux information, the full peak of the luminosity density can be explored.

6.2.2 Stellar mass, SFR plane

We can consider that a source is recovered if it has a true flux in at least one channel for the confusion-dominated maps (PHI2_1-PPI4; 47–235 μm), which is above the corresponding limiting flux in that channel from XID+. Revisiting the stellar mass-SFR plane for a single redshift bin of $1.5 < z \leq 2.0$ for the sources in the two prior catalogues used for the two XID+ runs (originally shown by the left-hand and right-hand panels in Fig. 4), we can identify which of these sources are recovered. The right-hand panels in Fig. 9 show the recovered sources meeting the above criteria from the two XID+ runs relative to the star-forming main-sequence (MS) from the literature. The left-hand panels show the sources that are recovered above the classical confusion limits determined by B24. For each M_*-SFR bin, the average number of channels in which the sources within that bin are recovered is also calculated and shown by the colour-scale. Additionally, an average SFR value for all sources that are detected in 2, 8, and 10 of the PHI2_1–PPI4 channels are also shown. The latter two ensure that at least two detections are made in the 96–235 μm channels and therefore robustly recovering a given galaxy in the FIR regime.

For the Wiener-filtered prior catalogue (top panels), XID+ recovers a comparable number of sources for this prior catalogue and redshift bin as those recovered above the classical confusion limits. This is due to the majority of the sources being detected in the shortest wavelength channel considered for the selection, PHI2_1 (47 μm), where the limiting flux from this run of XID+ is comparable to the classical confusion limit. However, XID+ is able to recover these sources in more channels. As such, it is able to accurately sample the FIR regime of galaxy SEDs (by detecting the galaxy and measuring its flux to an accuracy of better than 20 per cent in 8–10 channels in PHI2 and PPI bands) down to $\log_{10}$(SFR) ∼2–2.5 $M_\odot$ yr^{-1}. This provides an improvement of 0.5 dex compared to what can be recovered above the classical confusion limits. Also shown is the SFR of the knee of the FIR luminosity function at $z = 1.75$ from Magnelli et al. (2013), which has $\log(L_*) = 12.16\, L_\odot$

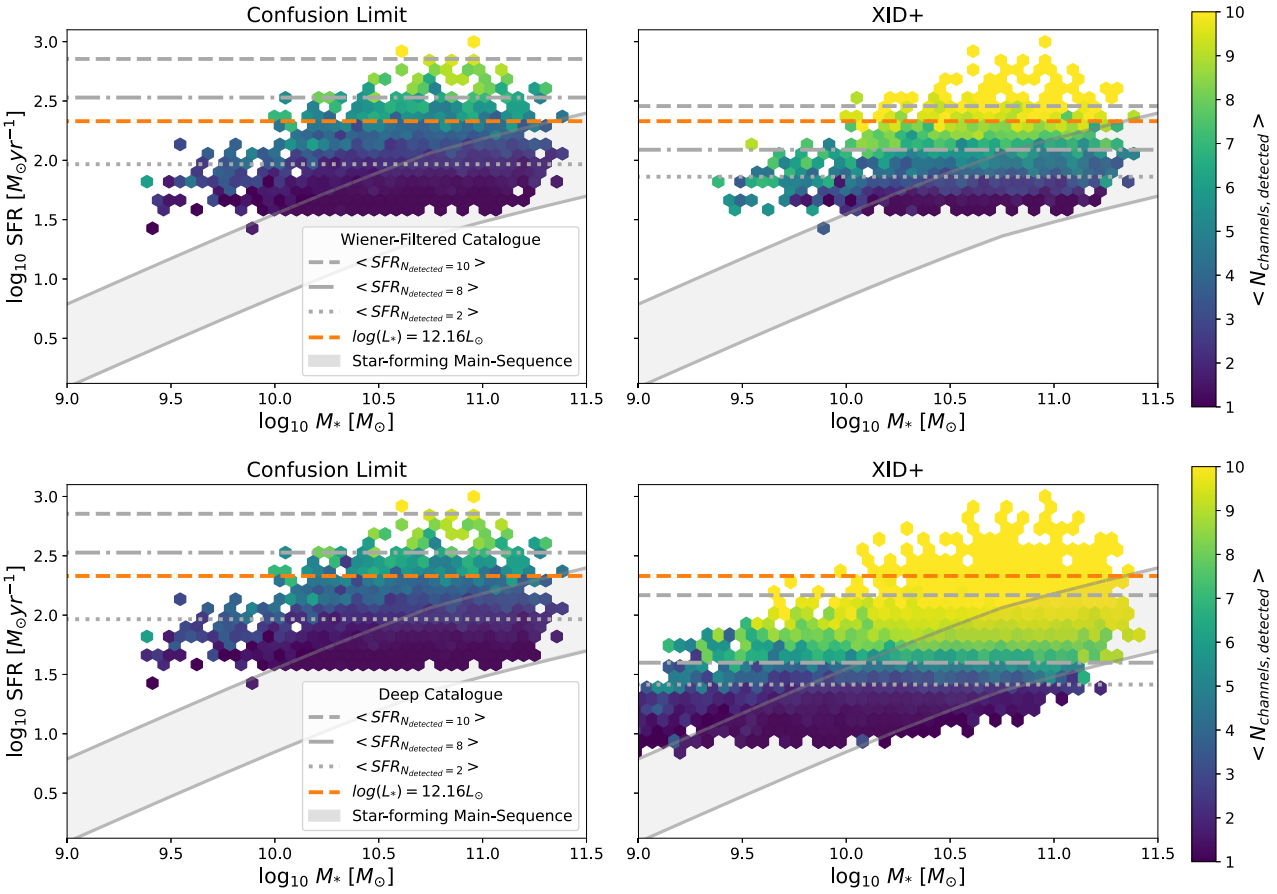

Figure 9. Locations of galaxies recoverable by XID+ in the stellar mass–SFR plane for a single redshift bin of $1.5 < z \leq 2.0$, colour-coded by the number of bands in which they could be detected. A galaxy is considered detectable if it has a true flux above the limiting flux in at least one channel for the confusion-dominated maps (PHI2_1-PPI4; 47–23 μm). The limiting fluxes are taken as the classical confusion limits from B24 for the top left-hand and bottom left-hand panels and as the limiting flux results from XID+ runs with the Wiener-filtered and Deep prior catalogues for the top right-hand and bottom right-hand panels, respectively. Colour-scale shows the average number of channels, which the sources within each M_*-SFR bin are detected in. Overplotted are the average SFR values for all sources that are detected in 2, 8, and 10 of the PHI2_1-PPI4 channels, shown by the dotted, dash–dotted, and grey-dashed horizontal lines, respectively. The orange-dashed horizontal line shows the SFR of the knee of the FIR luminosity function at $z = 1.75$ from Magnelli et al. (2013). The star-forming main-sequence curves from the literature are indicated by the shaded region. This shows that XID+ can recover multiband photometry into the main sequence with galaxies detected self-consistently by PRIMA (top right) and substantially spanning the main-sequence with deeper (external) prior catalogues (bottom right).

and a corresponding $\log(\mathrm{SFR}) = 2.33\ \mathrm{M_\odot yr^{-1}}$, using the conversion from Kennicutt & Evans (2012). XID+ is able to recover this knee of the FIR luminosity function in at least 8 of the 10 channels covering 47–235 μm.

For the Deep prior catalogue run of XID+ utilizing weak prior flux information, this is improved further, detecting sources in 8–10 channels down to $\log_{10}(\mathrm{SFR}) \sim 1.6$–$2.1$, which is approximately an order of magnitude below what is reached for sources above the classical confusion limits. Moreover, this run of XID+ is able to recover ∼3.6× more sources than those above the classical confusion limits for this prior source catalogue and redshift bin.

6.3 Obtaining prior flux information

For the runs of XID+, which have included prior flux knowledge, we have employed a toy model to represent the constraining power of the prior flux knowledge. In reality, these flux priors would need to be obtained via some modelling of the SED of the source. When PRIMA is launched, there will be a wealth of deep ancillary photometry available from contemporary missions and ground-based facilities. SED-fitting of this data could be performed to estimate the flux of the source in the particular channel map, which requires de-blending. The choice of SED modelling procedure as well as the type of ancillary data available to fit (e.g. radio and MIR photometry versus only UV/optical) will inevitably impact the accuracy of the modelling (Pacifici et al. 2023; Thorne et al. 2023). Moreover, even if the flux prior information is not constraining for specific sources and is only representative of typical galaxy populations, modelling these will still reduce the confusion noise. Exploiting prior flux information would still allow atypical galaxies to be detected by looking for cases where the posterior significantly departs from the prior distribution or where the model does not fit the data well through posterior predictive checking.

In addition to utilizing ancillary photometry, another approach that only requires data from PRIMAger is possible due to the probe's extensive spectral coverage and resolution. Source detection and photometry can be performed on the shorter-wavelength band PHI1 maps (i.e. $\lambda < 40$ μm), which are not confusion-dominated. Probabilistic SED fitting using an SED library (e.g. from CIGALE) can then be performed on these extracted fluxes to estimate, for

example, the fluxes of the sources in the next three channels (in ascending wavelength order), providing the flux priors to be used to de-blend the corresponding maps. This step-wise method can be repeated so that the reddest and most confused maps will have prior flux information, which is determined from the shorter wavelength maps. Applying this step-wise method and determining whether it can provide prior flux knowledge, which is sufficiently informative is beyond the scope of this paper, but we outline it here to be tested in the context of PRIMAger in future work.

7 CONCLUSIONS

In this work, we have shown that confusion mitigation methods utilizing positional priors successfully demonstrated on *Herschel* data sets will allow PRIMAger to reliably extract fluxes well below the classical confusion limits.

We have tested these mitigation methods on mock data that simulate a 1500 h deg^{-2} depth hyperspectal imaging survey with PRIMager, from 25–235 μm, using a sky, observatory, and instrument model that provides maps with realistic confusion and 'instrumental' noise.

We have demonstrated that we can produce catalogues of galaxies with high purity from the PRIMager images alone (i.e. blindly) using a Wiener-filter optimized to suppress both forms of noise. Specifically, we have produced catalogues with 95 per cent purity reaching 55–117 μJy in $S_{\rm obs}$ in the six PHI1 bands, where the majority of sources are first detected. This blind catalogue also reaches a completeness of ∼83 per cent on sources with $S_{\rm True} > \sigma_{\rm total}$ in PHI1 bands, with a source density 42 k deg^{-2} (or ∼0.5 sources per beam in PPI1 band).

We have then shown that we are able to accurately recover the fluxes of these high purity PRIMager sources from 25–235 μm with no prior flux information using the Bayesian probabilistic de-blending code XID+. We demonstrated that flux accuracy within 20 per cent of the true flux values is obtained below the confusion limits for all the confusion-dominated maps. A gain of a factor of ∼2 below the classical confusion limits (as estimated by B24) is achieved between 72–96 μm, as shown in Figs 6 and 7. This increases to a factor of ∼3 for 126–235 μm (the reddest channels in the PHI2 band). This allows PRIMAger to recover SEDs out to $\lambda = 126$ μm for sources at the knee of the infrared luminosity function for $z = 2$, as shown in Fig. 7.

We have also shown that even greater improvements are possible with the introduction of additional prior information, e.g. arising from the detection of and spectral energy distribution modelling of other wavelengths with data from other contemporary observatories. We have investigated the impact of increasing the source density of the prior position catalogue alongside varying prior flux knowledge on the flux modelling accuracy of XID+. De-blending of sources at high densities (>1 source per beam), or equivalently lower fluxes, benefits significantly from adding prior flux information to XID+. We show that with weak prior flux information (a Gaussian prior with dispersion equal to the flux) accurate fluxes for sources are recovered at $\lambda < 80$μm down to the instrumental noise level of the survey. This same catalogue and flux prior results in recovering fluxes about an order of magnitude below the classical confusion limit at 96–172 μm, and a factor of 6 below the classical confusion at 235 μm.

We have also shown that de-blending with XID+ allows a survey such as the one described for PRIMAger to detect and measure accurately source fluxes for galaxies, which contribute to the bulk of the IR luminosity density. Additionally, we have demonstrated that XID+ is able to sample the FIR regime of galaxy SEDs with accurate flux measurements in 8–10 of the 10 channels covering 47–235 μm for sources with log(SFR) ∼2–2.5 at $1.5 \leq z \leq 2.0$. This improves upon what can be achieved above the classical confusion limits by 0.5 dex, as shown in the top panel of Fig. 9. Most importantly, these observations are self-contained as the prior source catalogues can be obtained from the shorter wavelength PRIMAger maps, where confusion noise is not dominant, and are subsequently used to de-blend the longer wavelength maps and accurately measure source fluxes.

We have therefore demonstrated that imaging data from PRIMAger will not be limited by näive, classical confusion noise if deblending with XID+is employed. Accurate flux measurements below the confusion limits are therefore currently achievable using data from PRIMAger in a self-contained way.

Further improvement can also be achieved both by utilizing ancillary data to provide additional prior source positions and prior flux information and also with PRIMAger data along by using shorter wavelength data to provide improved priors by utilizing XID+ in a step-wise process as described in Section 6.3.

AUTHOR CONTRIBUTIONS

The contributions of the authors using the Contributor Roles Taxonomy (CRediT) were as follows: **James Donnellan:** Methodology, Software, Validation, Investigation, Writing – original Draft; **Seb Oliver:** Conceptualization, Supervision, Project Administration, Writing – Review & Editing, Funding acquisition; **Matthieu Bethermin:** Resources, Conceptualization, Writing – Review & Editing; **Longji Bing:** Methodology, Software, Validation, Investigation; **Alberto Bolatto:** Conceptualization, Writing – Review & Editing; **Charles M. Bradford:** Conceptualization, Writing – Review & Editing; **Denis Burgarella:** Writing – Review & Editing; **Laure Ciesla:** Conceptualization, Writing – Review & Editing; **Jason Glenn:** Conceptualization, Writing – Review & Editing; **Alex Pope:** Conceptualization, Writing – Review & Editing; **Stephen Serjeant:** Autoencoder deconvolution, writing – Review & Editing; **Raphael Shirley:** Writing – Review & Editing; **JD T. Smith:** Conceptualization, Writing – Review & Editing; **Chris Sorrell:** Autoencoder deconvolution, writing – Review & Editing.

ACKNOWLEDGEMENTS

James Donnellan and Chris Sorrell were supported by the Science and Technology Facilities Council, grant number ST/W006839/1, through the DISCnet Centre for Doctoral Training. Seb Oliver acknowledges support from the UK Space Agency through ST/Y006038/1. Longji Bing acknowledges funding from STFC through ST/T000473/1 and ST/X001040/1.

This paper makes use of ASTROPY (Astropy Collaboration et al. 2013) a community developed core PYTHON package for Astronomy.

DATA AVAILABILITY

The data from this paper is available from Sussex Figshare at https://doi.org/10.25377/sussex.26165806.

REFERENCES

Astropy Collaboration et al., 2013, A&A, 558, A33
Béthermin M. et al., 2017, A&A, 607, A89
Béthermin M. et al., 2022, A&A, 667, A156
Béthermin M. et al., 2024, preprint (arXiv:2404.04320)

Boquien M., Burgarella D., Roehlly Y., Buat V., Ciesla L., Corre D., Inoue A. K., Salas H., 2019, A&A, 622, A103
Burgarella D. et al., 2013a, A&A, 554, A70
Burgarella D. et al., 2013b, A&A, 554, A70
Calzetti D., Armus L., Bohlin R. C., Kinney A. L., Koornneef J., Storchi-Bergmann T., 2000, ApJ, 533, 682
Cardelli J. A., Clayton G. C., Mathis J. S., 1989, ApJ, 345, 245
Casey C. M., Narayanan D., Cooray A., 2014, Phys. Rep., 541, 45
Chapin E. L. et al., 2011, MNRAS, 411, 505
Condon J. J., 1974, ApJ, 188, 279
Dole H. et al., 2004, ApJS, 154, 93
Dole H. et al., 2006, A&A, 451, 417
Duivenvoorden S. et al., 2020, MNRAS, 491, 1355
Elbaz D. et al., 2011, A&A, 533, A119
Geach J. E. et al., 2017, MNRAS, 465, 1789
Genzel R., Cesarsky C. J., 2000, ARA&A, 38, 761
Gruppioni C. et al., 2010, A&A, 518, L27
Gruppioni C. et al., 2013a, MNRAS, 432, 23
Gruppioni C. et al., 2013b, MNRAS, 432, 23
Hauser M. G., Dwek E., 2001, ARA&A, 39, 249
Hurley P. D. et al., 2017, MNRAS, 464, 885
Kennicutt R. C., Evans N. J., 2012, ARA&A, 50, 531
Kessler M. F. et al., 1996, A&A, 315, L27
Kirkpatrick A., Pope A., Sajina A., Roebuck E., Yan L., Armus L., Díaz-Santos T., Stierwalt S., 2015, ApJ, 814, 9
Lauritsen L., Dickinson H., Bromley J., Serjeant S., Lim C.-F., Gao Z.-K., Wang W.-H., 2021, MNRAS, 507, 1546
Leja J. et al., 2022, ApJ, 936, 165
Leslie S. K. et al., 2020, ApJ, 899, 58
Long A. S., Casey C. M., Lagos C. D. P., Lambrides E. L., Zavala J. A., Champagne J., Cooper O. R., Cooray A. R., 2023, ApJ, 953, 11
Madau P., Dickinson M., 2014, ARA&A, 52, 415
Magnelli B. et al., 2013, A&A, 553, A132
Małek K. et al., 2018, A&A, 620, A50
Meurer G. R., Heckman T. M., Calzetti D., 1999, ApJ, 521, 64
Moullet A. et al., 2023, preprint (arXiv:2310.20572)
Narayanan D., Davé R., Johnson B. D., Thompson R., Conroy C., Geach J., 2018, MNRAS, 474, 1718
Neugebauer G. et al., 1984, ApJ, 278, L1
Nguyen H. T. et al., 2010, A&A, 518, L5
Oliver S. J. et al., 2012, MNRAS, 424, 1614
Pacifici C. et al., 2023, ApJ, 944, 141
Pearson W. J. et al., 2018, A&A, 615, A146
Pearson W. J., Wang L., van der Tak F. F. S., Hurley P. D., Burgarella D., Oliver S. J., 2017, A&A, 603, A102
Pilbratt G. L. et al., 2010, A&A, 518, L1
Puget J. L., Abergel A., Bernard J. P., Boulanger F., Burton W. B., Desert F. X., Hartmann D., 1996, A&A, 308, L5
Reddy N. A., Steidel C. C., Pettini M., Adelberger K. L., Shapley A. E., Erb D. K., Dickinson M., 2008, ApJS, 175, 48
Riccio G. et al., 2021, A&A, 653, A107
Riechers D. A. et al., 2013, Nature, 496, 329
Rowan-Robinson M. et al., 2018, A&A, 619, A169
Shim H. et al., 2023, AJ, 165, 31
Shirley R. et al., 2019, MNRAS, 490, 634
Shirley R. et al., 2021, MNRAS, 507, 129
Shivaei I. et al., 2017, ApJ, 837, 157
Speagle J. S., Steinhardt C. L., Capak P. L., Silverman J. D., 2014, ApJS, 214, 15
Thorne J. E., Robotham A. S. G., Bellstedt S., Davies L. J. M., 2023, MNRAS, 522, 6354
Viero M. P. et al., 2015, ApJ, 809, L22
Wang L. et al., 2021, A&A, 648, A8
Wang L. et al., 2024, preprint (arXiv:2405.18290)
Werner M. W. et al., 2004, ApJS, 154, 1
Zavala J. A. et al., 2023, ApJ, 943, L9

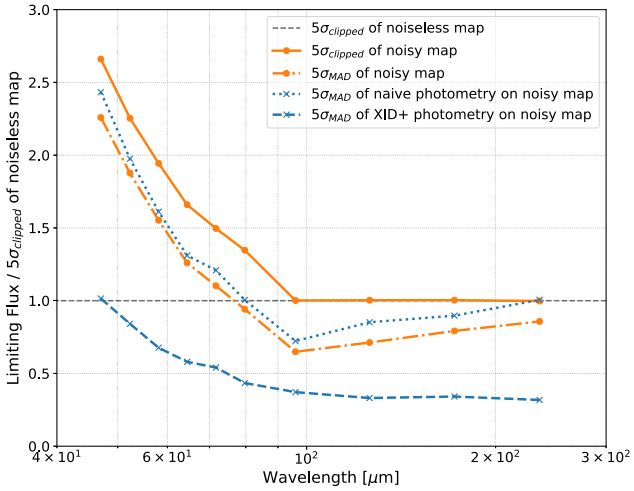

Figure A1. Comparison of different statistics used to measure noise in the simulated maps and the performance of different photometry methods for the 10 reddest PRIMAger filters (47–235 μm).

APPENDIX A: CHOICE OF LIMITING FLUX STATISTIC

Since confusion is highly non-Gaussian, any measurement of noise is very sensitive to the statistics being used. It is thus important to understand the relative contributions to improved performance arising from improved photometry through XID+ and through more appropriate statistics. In this appendix, we consider the impact of different statistics in measuring the fluctuations across the whole map (i.e. for measurements of sky or confusion noise) and then at the location of specific objects (i.e. for point source photometry).

In order to determine whether the limiting flux statistic introduced in Section 4.2.1 is a reasonable choice, we compare the results from XID+ to different measures of noise in the simulated maps.

First, we apply the same sigma-clipping process used by B24 to determine the classical confusion limits from the noiseless maps (as described in Section 2.1.1) to the maps that also contain instrumental noise. This provides an estimate of the total noise in the map and is shown by the solid orange line in Fig. A1. For the PPI maps, the instrumental noise is negligible compared to the confusion noise, and therefore the clipped-variance of the noisy map is comparable to that of the noiseless map. For the PHI2 maps, the clipped variance of the noisy map is greater than the confusion limits, as expected because the instrumental noise is non-negligible. This direct measurement of the total noise in the map is also greater than simply adding the two noise components in quadrature, as confusion noise is non-Gaussian.

Secondly, we estimate the MAD of the pixel values as a more robust estimator of the dispersion of the pixel values in the noisy maps (scaled by a factor of 1.4862, being the ratio between MAD and σ for a Gaussian distribution). This is shown in Fig. A1 as the dash–dotted orange line. It is clear that this statistic naturally returns a lower estimate of the noise than the clipped variance. This is partially because the MAD statistic ignores both the positive and negative tails, and while the clipping only removes the positive tail, but more importantly because the MAD statistic removes much more of the tails.

We now turn to consider the dispersion metrics at the locations of sources. To investigate this, we conduct a näive photometry to measure the fluxes of the Wiener-filtered catalogue sources in the noisy maps. This involves simply reading the value of the map at

the position on the source (as the maps are in units of mJy/beam). The MAD-based limiting flux statistic is then applied to these näive photometry measurements. The results are shown by the blue-dotted line in Fig. A1 and are consistent with the MAD measure of the total noise in the maps. Both, however, are systematically lower than the clipped variance measure of noise (∼10–20 per cent lower), implying that some of the gains from XID+ compared to the classical confusion limits are due to this choice of the statistic. Despite this, the results from XID+ remain below all of the measures of the total noise for all confusion-dominated maps.

APPENDIX B: ROBUSTNESS OF DECONVOLUTION TECHNIQUES

The impressive deconvolution achieved from the hyperspectral imaging is not unique to the XID+ algorithms. In this appendix, we demonstrate this through an alternative method for prior catalogue generation, using a machine learning model trained to super-resolve the full range of PRIMA bands into a single output. We use a denoising autoencoder adapted from that developed for *Herschel* SPIRE 500 μm imaging by Lauritsen et al. (2021). Unlike XID+, it does not assume the positions of a set of point sources extracted at shorter wavelengths as a Bayesian prior, but rather predicts the properties of the image from the training set of shorter wavelength data. The model was trained using cut-outs of the simulated hyperspectral PRIMAger imaging from this paper, with the target resolution for the longest wavelength data being that of the shortest wavelength imaging, i.e. a resolution improvement of a factor of approximately five. Fig. B1 shows the results of this deconvolution in a segment of the simulated image; also shown is the PRIMA catalogue generated target image for the same region of sky. The model has never been exposed to this target image. A comprehensive analysis of the statistical properties of this alternative PRIMA deconvolution is deferred to a later paper, though it is clear that the deconvolution capacity is a general property of PRIMA's hyperspectral imaging and not simply specific to prior-based deblending algorithms.

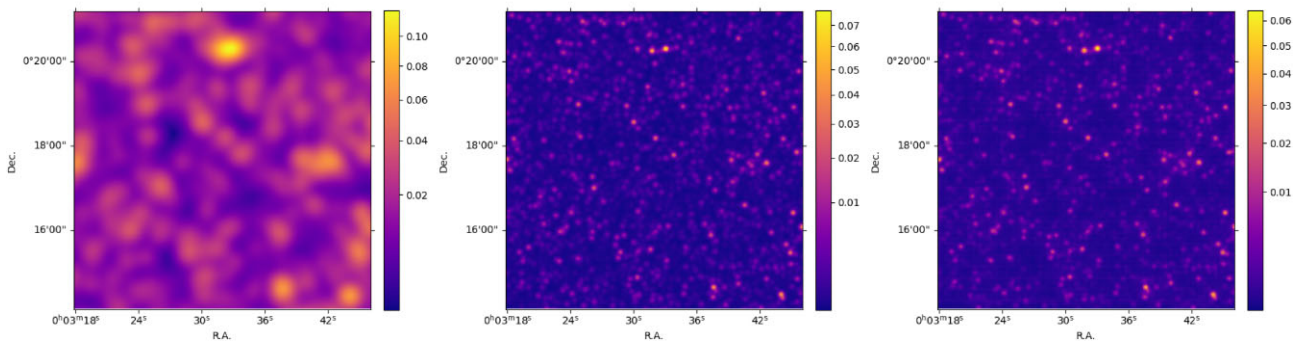

Figure B1. This figure shows 424 × 424 arcsec^2 postage stamps of the simulated 235 μm PRIMA SIDES image (left) compared to the autoencoder predicted image (right), showing a resolution increase of around a factor of 5. Also shown is the catalogue generated 'target' image (centre), which has never been seen by the predicting model. The flux scale is in Jy/beam. A comparable deconvolution product can be created from the XID+ prior-based deblending.

This paper has been typeset from a TEX/LATEX file prepared by the author.